Supplementary Information (SI) for Green Chemistry.

Mechanochemically activating lepidolite to allow easier lithium extraction and safer thallium handling through alunite formation

Chao Wang [ab] *, Xueyan He [c], Junwei Huang [d], Ting Jiang [d], Huimin Hu [e], Qiwu Zhang [b]

a Chinese Academy of Sciences, Ganjiang Innovation Academy, Ganzhou 341000, China

b School of Resources and Environmental Engineering, Wuhan University of Technology, Wuhan 430070, China

c Department of Obstetrics and Gynecology, The Sixth Hospital of Wuhan, Affiliated Hospital of Jianghan University, No.168, Xianggang Road, Jiangan District, Wuhan, Hubei 430015, China

d Zhengzhou Institute of Multipurpose Utilization of Mineral Resources, CAGS, Zhengzhou 450006, China

e State Environmental Protection Key Laboratory of Water Environmental Simulation and Pollution Control, South China Institute of Environmental Sciences, Ministry of Ecology and Environment, Guangzhou 510655, P.R. China

* Corresponding author.

Chao Wang E-mail address: cwang@gia.cas.cn; Tel: +86-18879738617

Chinese Academy of Sciences, Ganjiang Innovation Academy, Ganzhou 341000, China

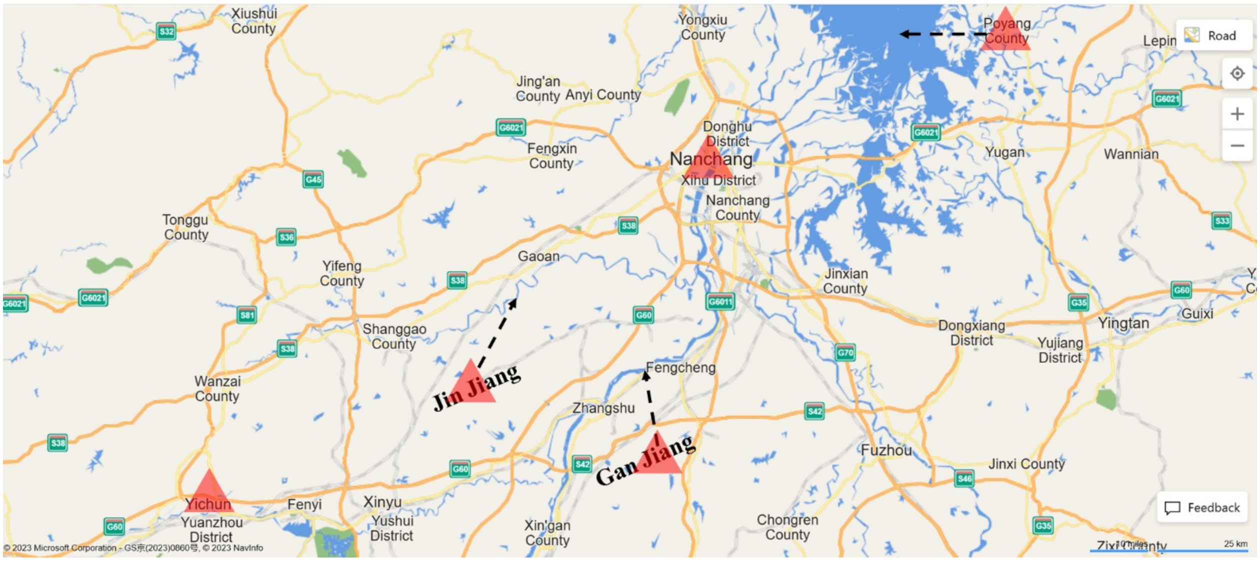

Figure. S1. Satellite Distribution Map of Jinjiang River Poyang Lake Basin (The part marked in red indicates the cities in Jiangxi Province where the Gan River and Poyang Lake are the main sources of drinking water [1, 2].)

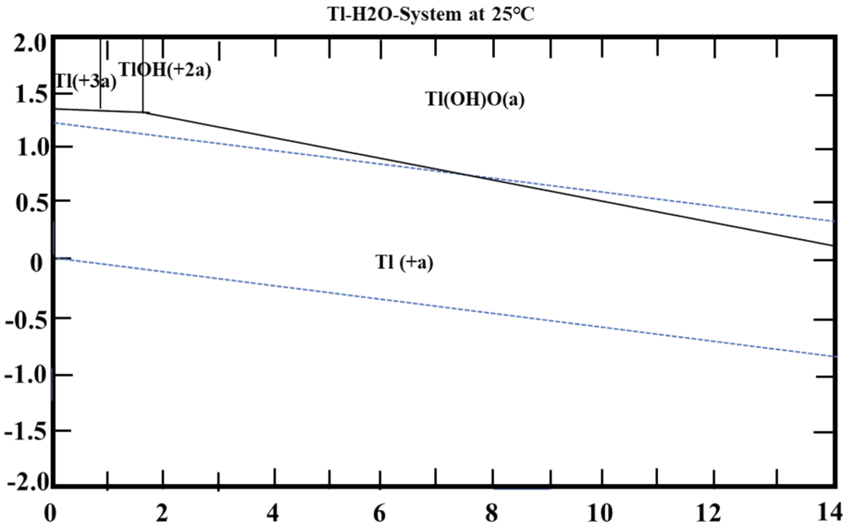

Figure. S2 Eh-pH diagram of thallium(I) in the Tl–H_2O system solution.

(According to the previous literature [3-5], the Eh-pH diagram (Figure. S2) shows that Tl^+ species dominates under most normal conditions with the pH at a range of 0–13 and the Eh at a range of − 0.85–1.35 V)

Table. S1 The strengths and weaknesses of various approaches：

Methods	Removal rate	initial Tl$^+$ concentration	Mechanism	Advantage	Disadvantage	Reference
Prussian blue-Fe_3O_4@TRG NPs	98%	200 mg/L	Ion-exchange	Recyclable	Complex to make	[6]
Prussianblue@polytetrafluoroethylene hybrid membranes	97%	0.5mg/L	Ion-exchange	Greater throughput	expensive	[7]
Fe_3O_4@TiO_2 decorated RGO nanosheets	94.7%	8.5 mg/L	Adsorption	Recyclable	Complex	[8]
Titanium dioxide interface	90.2%	40 mg/L	Adsorption	Recyclable	Introduction of contamination	[9]
Poly aluminum chloride	99.97%	1mg/L	Adsorption	High efficiency	High cost	[10]
Al can waste with amendments of Fe	98%	100 µM	Oxidative precipitation	Simple procedure	Fe/Al ions contamination	[10,11]
Fe^0-PS	98%	50 mg/L	Oxidative precipitation	Suitable for industrial wastewater	Fe contamination	[12]
$KMnO_4$	＞90%	30 µM	Oxidative precipitation	high efficiency	Mn-pollution	[13]
Bioelectricity generation	80.5%	5 mg/L	Electrochemical oxidation	Coupling with electricity generation	Secondary pollution	[13]
S- zero-valent Mn	97.47 ± 0.99%	20 mg/L	Sulfidation precipitation	wide range of applications,	Secondary S-pollution	[14]
Alunite structure	**＞98.5%**	**3.5-1000 mg/L**	**Co-precipitation**			**This study**

Text S1. An introduction to the activation of minerals by mechanochemical:

The mechanochemical method refers to the application of mechanical energy by ball milling to condensed substances such as solids and liquids employing shear, abrasion, impact, and extrusion to induce changes in their structure and physicochemical properties and to induce chemical reactions [15-17]. In the previous research, the application of mechano-chemical activation of non-metallic minerals such as serpentine and calcite to the treatment of heavy metals in the environment has been reported.

Components	Li_2O	Al_2O_3	SiO_2	Na_2O	K_2O	CaO	MnO_2	SO_2
(%)	2.22	27.23	58.55	1.07	8.40	0.18	1.33	0.36
Components	BaO	P_2O_5	ZrO_2	PbO	Fe_2O_3	SrO	SnO_2	Total
(%)	0.013	0.063	0.030	0.018	0.075	0.030	0.021	100%

Table. S2 chemical composition of the lepidolite sample

Table. S3 the characteristic particle sizes were estimated by interpolation:

Size fraction (mm)	Mass proportion (%)	Cumulative passing (%)
<0.074	12.26	12.26
0.074–0.1	8.18	20.44
0.1–0.15	38.42	58.86
0.15–0.2	12.9	71.76
>0.2	28.24	100

Table. S4. Particle size distribution parameters of the lepidolite sample

Sample	D10 (μm)	D50 (μm)	D90 (μm)
Lepidolite	60	140	220

Text S2. Chemicals and Reagents

All commercially available analytically pure agents acquired were not further purified. The corresponding concentrations of the required ionic solutions were configured by diluting the mother liquor using ultrapure water of 18.2 MΩ·cm [18]. The gibbsite ($Al(OH)_3$) is a pure chemical agent, purchased from Guangzhou Chemical Reagent Co., Ltd. (China). All the above agents were analytically pure and required no further treatment, and the solution configured in this study used deionized water as the solvent.

S2.1 Tl^+ stock solutions Tl^+ stock solution (1 g/L) was prepared with 18.2 MΩ·cm of ultrapure water. Briefly, 1.304 g $TlNO_3$ was directly dissolved in ultrapure water to gain the 1 g/L Tl^+ stock solution. Store stock solution in a refrigerator at 4°C protected from light. The concentration Tl^+ stock solutions were employed by inductively coupled plasma mass spectrometry and atomic absorption spectrum (ICP-MS and AAS) [19,20].

S2.2 Li^+ stock solution 1.1 g Li_2SO_4 was directly dissolved in 0.1L of ultrapure water to prepare the 10 g/L of Li(I) stock solution, similarly, the Li(I) stock solution was stored in a refrigerator at 4 °C.

S2.3 K^+ stock solution 10 g/L K_2SO_4 stock solution was prepared by dissolving 22.31 g K_2SO_4 into 1L ultrapure water.

S2.4 Configuration of 25 g/L K_2SO_4 as masking agent The Li^+ concentration test requires the addition of 25 g/L of K_2SO_4 as a masking agent for the experiment. Dissolve 2.5 g of K_2SO_4 in 100 mL of deionized water to make a 25 g/L solution of masking agent. When AAS was used to test the Li^+ concentration, 1 mL of 25 g/L K_2SO_4 was added as a masking agent.

S2.5 Configuration of 10 g/L Cs_2SO_4 as masking agent the K^+ concentration test requires the addition of 10 g/L of Cs_2SO_4 as a masking agent for the experiment. Dissolve 1.0 g of Cs_2SO_4 in 100 mL of deionized water to make a 10 g/L solution of masking agent. 1 mL 25g/L Cs_2SO_4 was added as a masking agent for K^+ concentration.

S2.6 Adjustment of the initial pH of the solution Before the reaction, the different initial pH of the solution is regulated by 0.1 mM H_2SO_4 as well as NaOH.

Text S3. Ball milling activation details

Mechanochemical activation of gibbsite was performed on a planetary mill (Pulverisette-7, Fritsch, Germany), equipped with a pair of zirconia grinding troughs with a total volume of 45 cm^3 and 7 zirconia grinding balls with a diameter of 10 mm (Figure. S3a).

S3.1 Activation process of lepidolite by ball milling

2 g of lepidolite was mechanically activated in a grinding tank at different grinding speeds, and the activation time was set to 2 h.

S3.2 Ball milling activation gibbsite process

The raw gibbsite ore with a total mass of 2 g was directly injected into the grinding tank (Fig. S3b) against grinding operation with various grinding parameters [21,22].It can be seen from the XRD pattern that the diffraction peaks of the gibbsite gradually become weaker as the ball milling intensity increases from o to 600 rpm. Specifically, according to the calculation rule of Scherrer's formula, the grain size D of the gibbsite samples decreases gradually with the increase of ball milling speed, shrinking from 57.5 nm at 0 rpm to 3.4 nm at 600 rpm, respectively, as shown in Table S3.

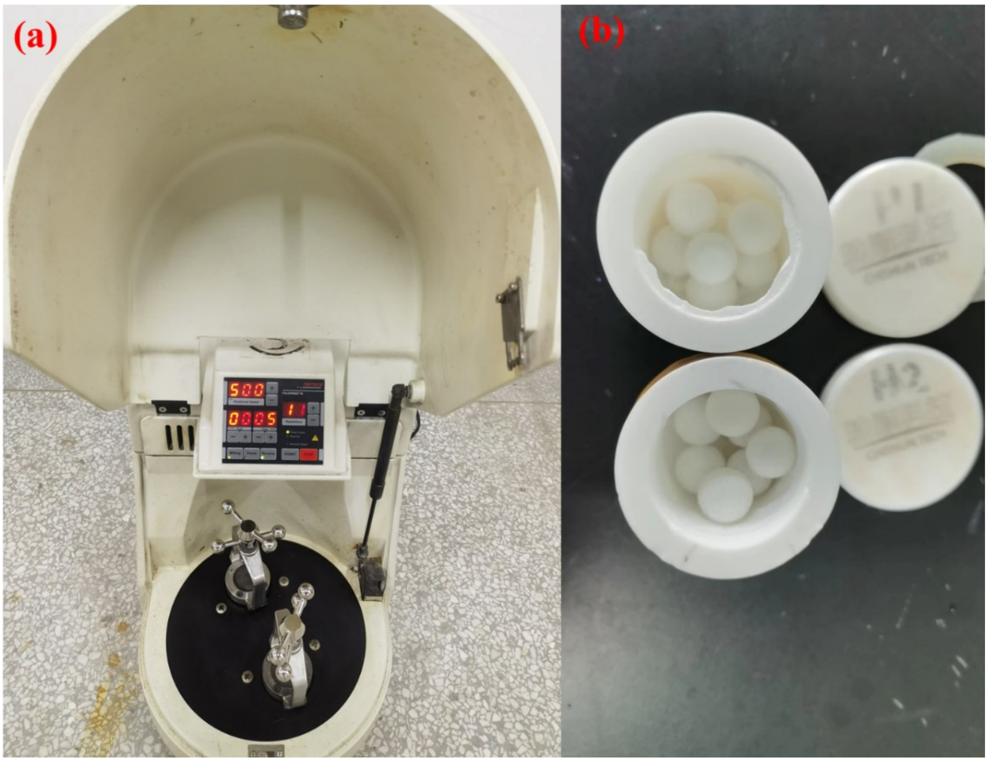

Figure. S3 (a) planetary ball mill (b) Zirconium tank

Figure. S4 the actual physical map of lepidolite ore

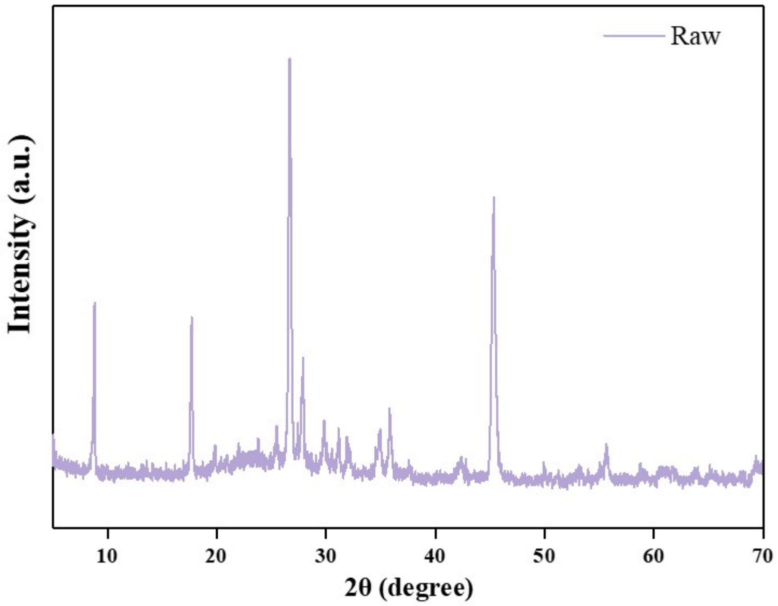

Figure. S5 XRD of actual lepidolite ore

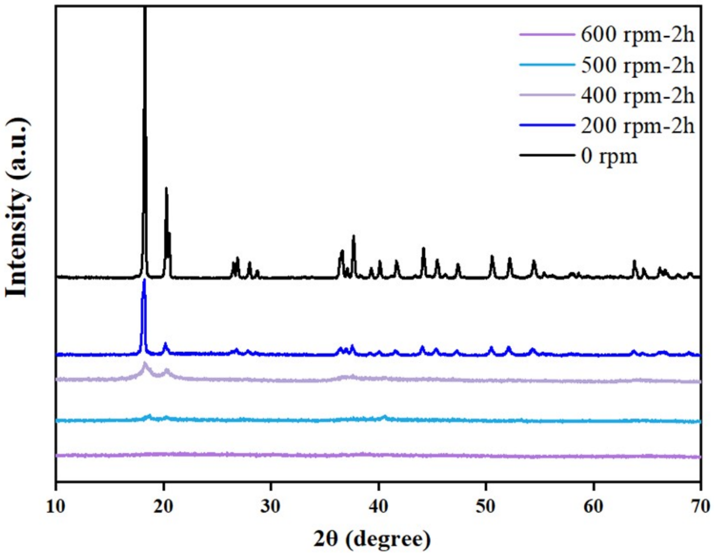

Figure. S6 XRD patterns of Gibbsite obtained under the activation of mechanochemistry ball milling (0, 200 rpm, 400 rpm, 500 rpm, 600 rpm)

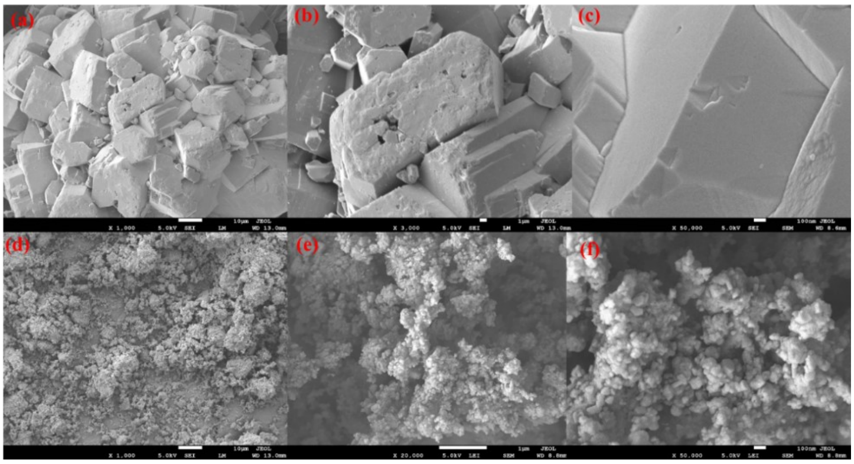

Figure. S7 Comparison of morphology analysis before and after ball milling at different scales: (a)-(c); 10 μm, 1 μm and 200 nm before ball milling; (d)-(f) 10 μm, 1 μm and 200 nm after ball milling

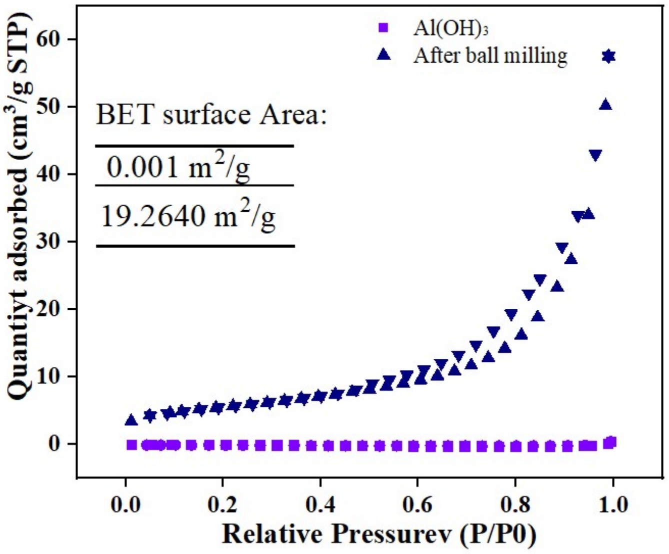

Figure. S8 Comparison of the specific surface area before and after ball milling

Table. S5 Tl^+ Concentrations in leachates of Various acids

Acid concentration (%)	Tl^+ Concentration(ug/L)	Acid type	Tl^+ Concentration (ug/L)
0	0.53	water	0.53
1	21.15	H_2SO_4	51.13
2	42	HNO_3	50.15
3	48.18	H_3PO_4	48.28
4	51.25	citric	47.19
5	52.21	acetic	22.15

Test S4 Morphological changes due to ball milling

Figure S9 shows the morphology of the sample in different magnifications (10 μm, 1μm, and 100 nm) compared with the sample obtained under the ball milling conditions at 500-2h. It can be found in Figure. S7(a)-(c) that the surface of the raw gibbsite particles is relatively smooth, showing a block structure with a large particle size. However, the morphology of the sample after ball milling (500 rpm-2h) shows a huge change, which is reflected in the significant reduction of particles, and the surface is a little rough and agglomerated with each other (Figure. S7 (d)-(f))

Test S5 BET changes due to ball milling

BET was applied to further investigate the specific surface area of samples in Figure. S8. The result demonstrates that the specific surface area of the gibbsite increases from 0.001 to 19.264 after ball milling, and the greatly increased specific surface area also facilitates the subsequent immobilization of K(I).

Text S6. Conditions for acid leaching

S6.1 Effect of ball milling speed on acid leaching

The lepidolite samples were activated at different ball milling speeds (0, 300 rpm, 400 rpm, 500 rpm, 600 rpm,) and then placed in 4% H_2SO_4 for stirring, and the concentration of Li^+/K^+ in the solution was tested by atomic absorption.

S6.2 Effect of acid concentration

The ball milling conditions were set at 500 rpm-2 h, and the lepidolite activated under these conditions was placed in 0, 1%, 2%, 3%, 4%, and 5% H_2SO_4 for 24 hours of leaching. the concentration of Li^+/K^+ in the solution was tested.

S6.3 Effect of different acid

According to S6.2, the ball milling conditions were set at 500-2h and the acid leaching concentration at 4%. Comparison of leaching of different acids on lepidolite, including H_2SO_4, HNO_3, H_3PO_4, citric acid, and acetic acid.

S6.4 Effective acid leaching temperature

The optimum acid species derived from S6.3 was citric acid, and the effect of reaction temperature on the leaching of Li^+/K^+ was observed. The reaction temperatures were set to 25 °C, 45 °C, 55 °C, 65 °C and 85 °C.

S6.5 Co-ground mineral species

In actual minerals lithium mica is often associated with different other minerals, so feldspar, calcite, muscovite and quartz were ball-milled at 500 rpm-2h in a mass ratio of 1:1, respectively. The resulting co-ground samples were continued to be leached at 25 °C under 4% citric acid.

Text S7. Various parameters on the removal rates of K^+ or Tl^+ from modeled wastewater

The activated $Al(OH)_3$ and $Al_2(SO_4)_3$ were added to the mother liquor configured in 2.3.2. After reaction, the treated solution was filtered by a 0.22 μm membrane and the residual concentration of Tl^+ was determined by Atomic Absorption Spectrometry (AAS) and Inductively Coupled Plasma Mass Spectrometer (ICP-MS, ELAN 9000 Perkin Elmer, USA).

S7.1 Grinding parameters

The effects of different ball milling speed and ball milling time on activated $Al(OH)_3$.

The $Al(OH)_3$ with a total mass of 2 g was directly injected into the grinding tank, and the grinding operation with different grinding parameters was carried out. The ball milling speed was set to 0 ~ 600, and the grinding time was set to 0 ~ 2 h.

S7.2 Effect of reaction temperature

The reaction temperatures required for the experiment are extremely demanding, and the reaction temperatures were set at 20-90 °C.

S7.3 The molar ratio of $Al(OH)_3$:$Al_2(SO_4)_3$:K_2SO_4

The ratios of $Al(OH)_3$:$Al_2(SO_4)_3$:K_2SO_4 were set to different molar ratios according to the Eq. (S2). The ratios of 0:1:1, 4:1:1, 8:1:1, 12:1:1, 8:0:1, 8:1:1, 8:2:1 8:3:1, 8:2:0, 8:2:0.5, 8:2:2, 8:2:3 and 8:2:4 appeared in Figure. 4a-4c.

S7.4 Effect of initial pH

The initial pH of the solution was adjusted to 0.86-12.6 by the H_2SO_4 and NaOH in Figure. 4d.

S7.5 Effect of solution volume

The solution volume is one of the factors that affect the collision probability of each ion. The solution volume is changed to 25-400 mL (Figure. 4e) to observe the concentration changes of Li^+, K^+, and Tl^+ in the solution.

S7.6 Effect of initial Tl^+ concentration

The initial concentration of Tl^+ required during the test was 3.5-1000 mg/L, which was diluted by the reserve solution in S2.1.

Test S8. X-ray absorption spectroscopy

Data collection and extraction

X-ray absorption spectra (XAS) of the samples at Tl LIII-edge, including X-ray absorption near edge structure (XANES) and extended X-ray absorption fine structure (EXAFS), were collected at the TPS44A1 beamline at the National Synchrotron Radiation Research Centre (NSRRC) in Taiwan. XANES spectra of all samples were energy-selected at room temperature using either a Si(111) double-crystal monochromator (SNBL, DUBBLE, SAMBA) or a Si(111) channel-cut monochromator (SuperXAS monochromator (SuperXAS). Spectra of $TlNO_3$ measured in transmission mode and used for energy calibration in terms of Se(0), which has a maximum energy value of 12658 eV for the first-order derivative of Se(0). Samples with Tl-concentrations of 0.2-1% were measured in fluorescence mode, while samples with Tl-concentrations above 1% were measured in transmission mode. The final XANES datasets of Tl sorption to 200-alunite, and 1000-alunite were recorded at the Super-XAS beamline. In addition to the XANES spectrum, the EXAFS spectrum was measured. EXAFS spectra of selected samples were recorded at 20 K using a liquid helium cryostat at the SAMBA beamline to compare changes in the coordination form of Tl in the structure. The software package Demeter was used to extract normalized XANES and EXAFS spectra for analyzing the oxidation state of Tl in selected samples by linear combination fitting (LCF) and for analyzing the local coordination role shaping of Tl in selected samples by shell fitting to the corresponding EXAFS spectra. The normalized XAS spectra were obtained by setting the edge energy E_0 to 12658 eV, fitting the data in a straight line with E_0 at -100 to +35 eV, and fitting a second-order polynomial to the data at the edges +35 to 120 eV in order to achieve the edge stepnormalization of E_0 and the flattening of the XANES spectra.

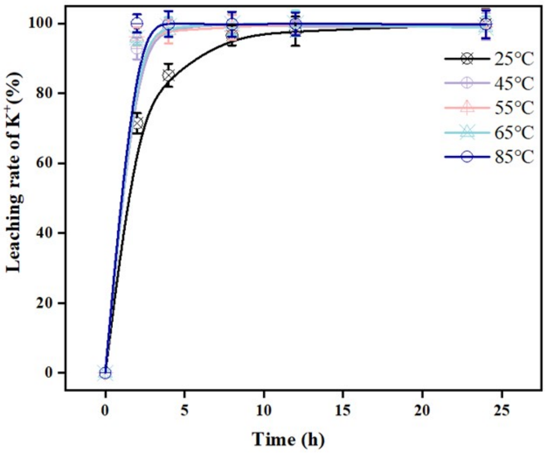

Figure. S9 Effect of temperature on K^+ release from lepidolite

Table. S6: Element analysis of activated lepidolite (500 rpm-2h) after leaching in 4% H_2SO_4

Element	Li	Al	Si	Na	K	Ca	Mn	S
	104.8	1436.07	270.7	74.67	659.7	19.40	80.11	7.6
Concentration (mg/L)	Ba	Sr	As	Fe	Mg	Sn	Total	
	0.11	1.75	0.69	8.01	11.19	1.71	100%	

Table. S7: Element analysis of activated lepidolite (500 rpm-2h) after leaching in 4% critical acid

Element	Li	Al	Si	Na	K	Ca	Mn	S
	110.5	1487.53	74.57	79.38	762.99	21.1	80.11	14573.17
Concentration (mg/L)	Ba	P	Sr	As	Fe	Mg	Sn	Total
	0.065	22.11	1.78	0.33	8.5	11.7	0.33	100%

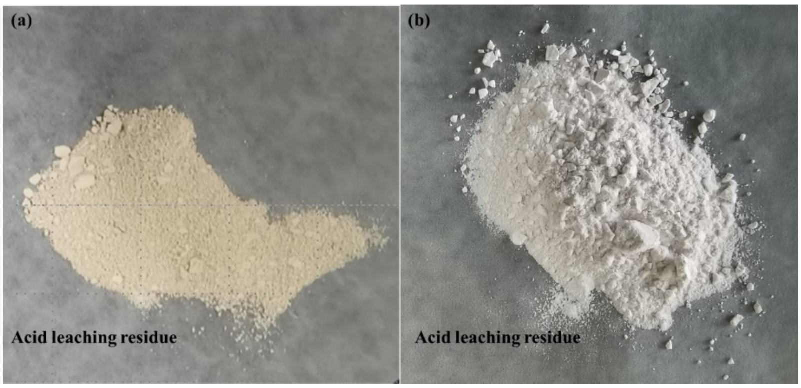

Figure. S10: Graph of products after acid leaching

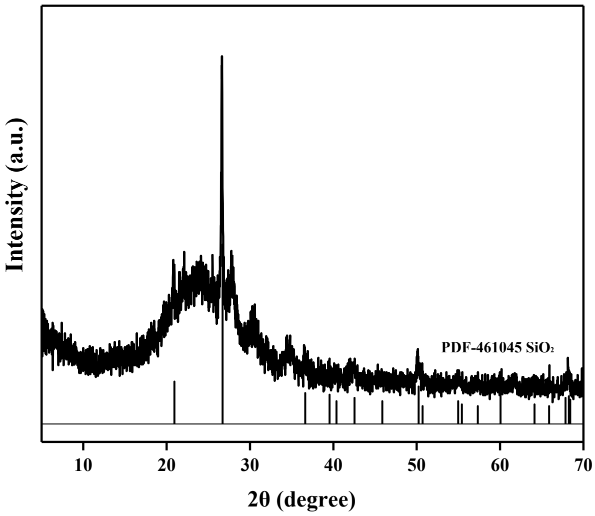

Figure. S11: XRD pattern of the product after acid leaching

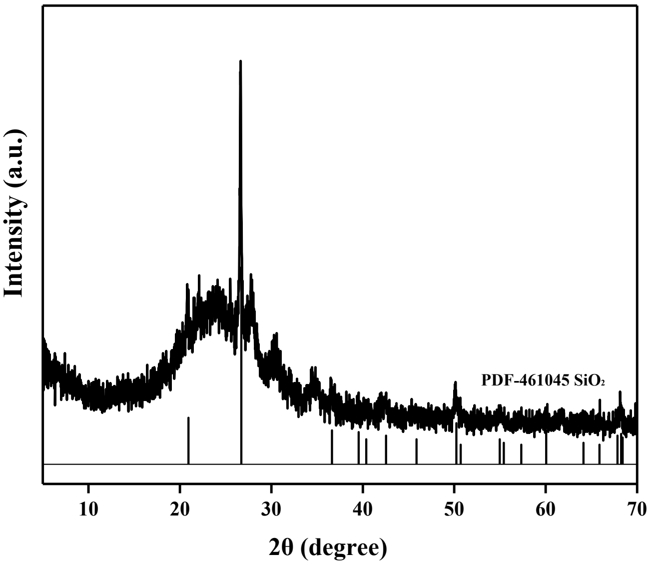

Figure. S12: XRD pattern of the product after citric acid leaching

Text S9. Cost comparison between mechanochemical leaching and conventional roasting for lepidolite processing

To provide a more comprehensive economic perspective, the cost of the mechanochemical leaching step (ball milling + 4% H_2SO_4 leaching) was estimated and compared with that of conventional high-temperature roasting. As summarized in Table S10, the material and energy costs for the mechanochemical route are approximately \$4.08 per cubic meter of leach solution, based on an estimated energy consumption of 25 kWh/t ore and a solid-to-liquid ratio of 1:100. This cost covers the mechanical activation and dilute acid leaching steps. For conventional roasting processes, the cost structure is substantially different. High-temperature roasting (800–1000 °C) requires significant thermal energy input, typically derived from fossil fuel combustion, in addition to the use of concentrated H_2SO_4 and subsequent off-gas treatment to capture volatile pollutants such as Tl. According to literature reports and industrial practice, the total operating cost for conventional roasting-based lithium extraction from lepidolite ranges from \$15 to \$30 per cubic meter of leach solution, depending on energy prices, acid consumption, and waste treatment requirements.

Table S8：Cost estimation and calculation process of two methods

Cost Factor	Conventional Roasting	This Work (Projected Industrial Scale)
Energy consumption	250–350 kWh/t	25 kWh/t
Energy cost (USD/t)	\$25–35 (at \$0.10/kWh)	\$8–12 (at \$0.10/kWh)
Acid consumption	30–50% H_2SO_4	4% citric acid
Acid cost (USD/t)	\$40–80	\$4
Operating temperature	800–1000°C	25°C (room temperature)
Equipment wear	High (high-temperature corrosion)	Low (ZrO_2 media, <0.8% contamination)
Wastewater treatment	High volume, complex	Low volume, simpler
Tl volatilization control	Required (expensive)	Not required
Total	\$45.60 /m^3	\$4.08 /m^3

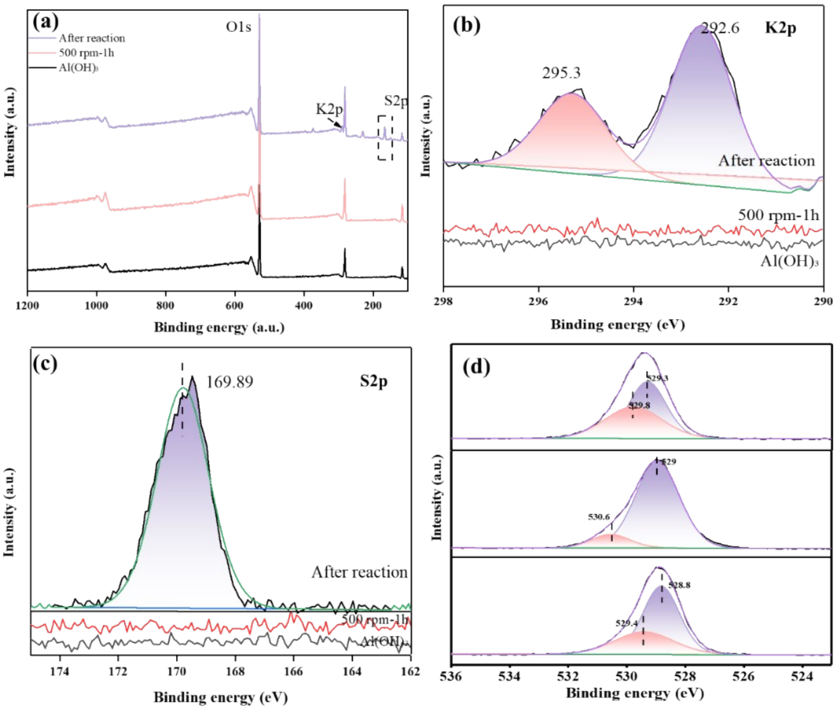

Figure. S13: XPS comparison of products (a) survey (b) K2p (c) S2p (d) O1s

Test. S10 XPS analysis of coprecipitated products and original samples

As shown in Figure. S13, XPS spectra of the samples before and after milling and after immobilization of K$^+$ and Tl$^+$ were analyzed to further reveal the mechanism of Li$^+$-K$^+$-Tl$^+$ separation. In the survey spectra, two new elemental signals, S2p and K2p, appeared in the samples after the reaction with K$^+$, showing signals of a clear shift of gibbsite to alunite after the reaction. The peaks at 295.3 eV and 292.6 eV are attributed to the K2p split, while 169.89 eV exhibits the S2p split [23,24].

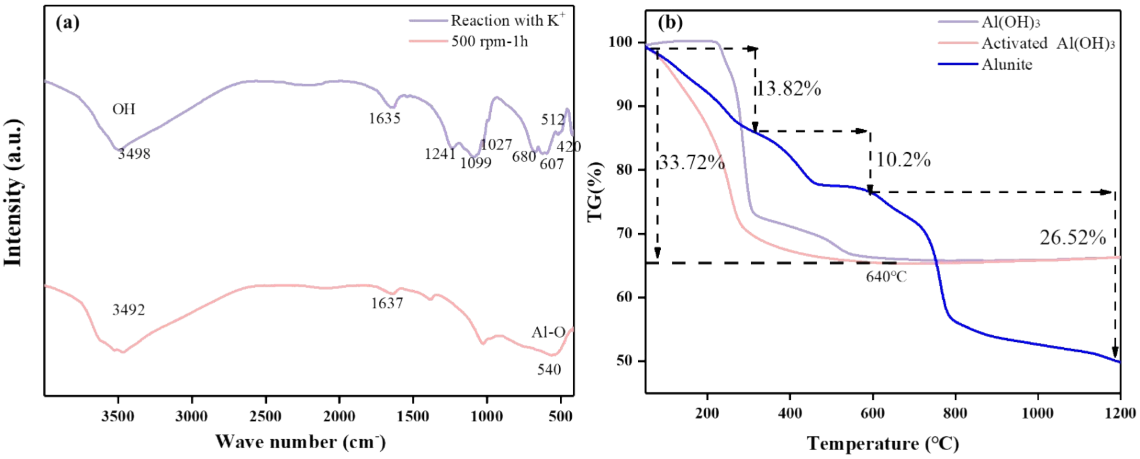

Figure. S14 characterization of Al(OH)$_3$ before and after reaction with K$^+$/Tl$^+$.(a)FT-IR and (b)TG (reaction conditions: 500 rpm-2h, 90°C-2h)

Test. S11 Comparison of IR and TG analyses of co-precipitated products with the original samples

Figure S14 exhibits the FTIR and TG analysis of gibbsite before and after reaction. with the K$^+$. The FTIR spectra of activated gibbsite and alunite slag are significantly different and the detailed variation details are given in Figure. S14a Further, the samples of gibbsite before and after ball milling and alunite precipitate were analyzed by TG-DSC as shown in Figure. S14b. The total mass lost before and after ball milling is close to 33.72% before 640°C, and then the mass loss is almost constant due to the complete conversion of $Al(OH)_3$ to Al_2O_3 (as shown in eq. S3), which is very close to the theoretical value, indicating that the sample of $Al(OH)_3$ are very pure and there are no other impurity phases present. Compared with the thermogravimetric results of $Al(OH)_3$, the mass loss of the product after the reaction of gibbsite with K^+/Tl^+ is about 13.82 % in the range of 0°C-300°C, which is because part of gibbsite is still retained in the residue. Also, the mass loss of the samples was 10.2% between 300 °C-600 °C, suggesting a loss of hydroxyl groups in alunite, whereas a larger mass loss (about 26.52%) was observed between 800°C-1200°C, which attributed to the mass loss due to decomposition of sulfate in the samples. Taken together, the results of the TG analysis of the samples agreed with the results obtained from the FT-IR analysis of the samples.

$$3Al(OH)_3=Al_3O_2+3H_2O \qquad \text{Eq. (S3)}$$

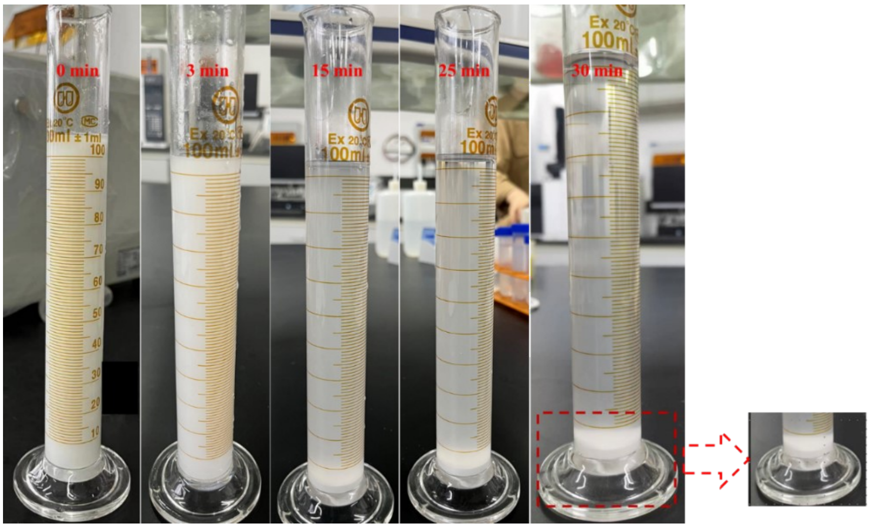

Figure. S15: Study of Sedimentation Properties

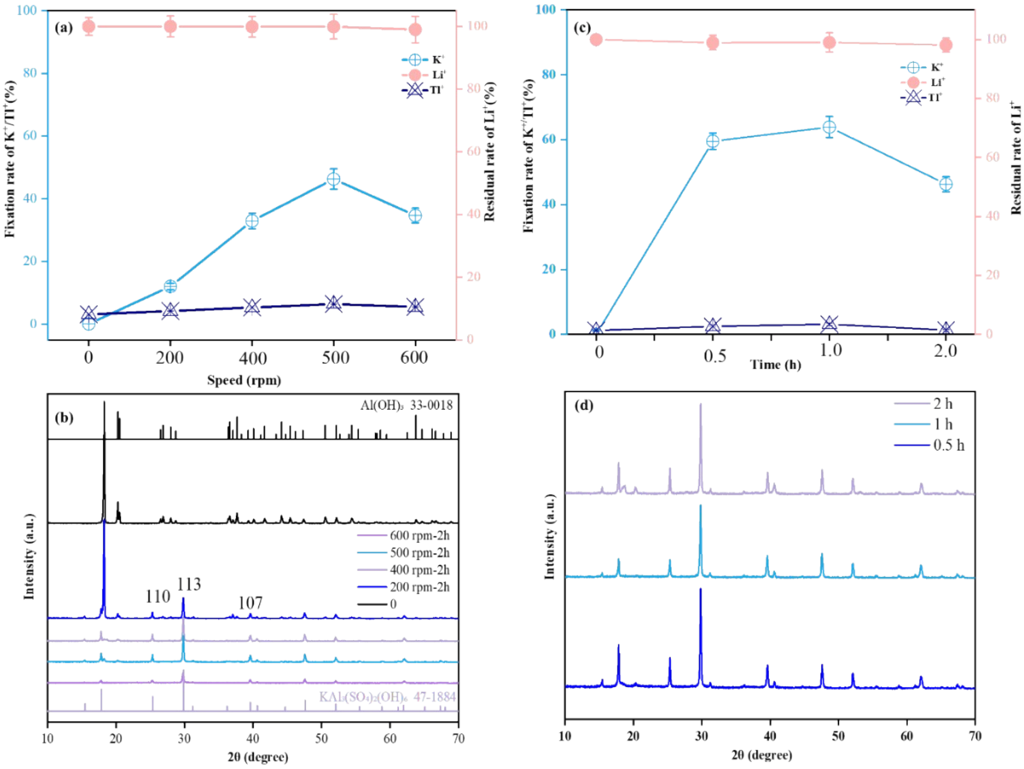

Figure S16: (a) and (b): Effect of ball milling speed on $Al(OH)_3$ and XRD pattern of the corresponding residue after the reaction; (c) and (d) Effect of ball milling time on the reaction and XRD patterns of the corresponding products (Reaction conditions: The volume of the solution is 50 mL; the molar ratio of $Al(OH)_3/Al_2(SO_4)_3/K_2SO_4$ is 4:1:1)

Test. S12: Effect of ball milling time on the reaction

Figure. S16 shows the K(I) uptake within 2h using different ball milling times (0-2h) of activated gibbsite, further confirming a relatively optimal activated time of 1h with a K(I) immobilize capacity of as high as 64.26%. Based on the above quantitative data, the XRD of the post-reaction residue was compared in Figure. S16b. The XRD patterns of the reacted samples obtained at ball milling times of 0.5 h or 1 h are almost pure phase $KAl_3(SO_4)_2(OH)_2$, which suggests that the reaction between activated $Al(OH)_3$, $Al_2(SO4)_3$ and K(I) is complete. Alternatively, the XRD pattern of the sample obtained at a milling time of 2h shows weak diffraction peaks on the (002) and (110) crystal planes of $Al(OH)_3$ in addition to the phase of $KAl_3(SO_4)_2(OH)_2$, suggesting that the activation time of 2h leads to $Al(OH)_3$ agglomeration.

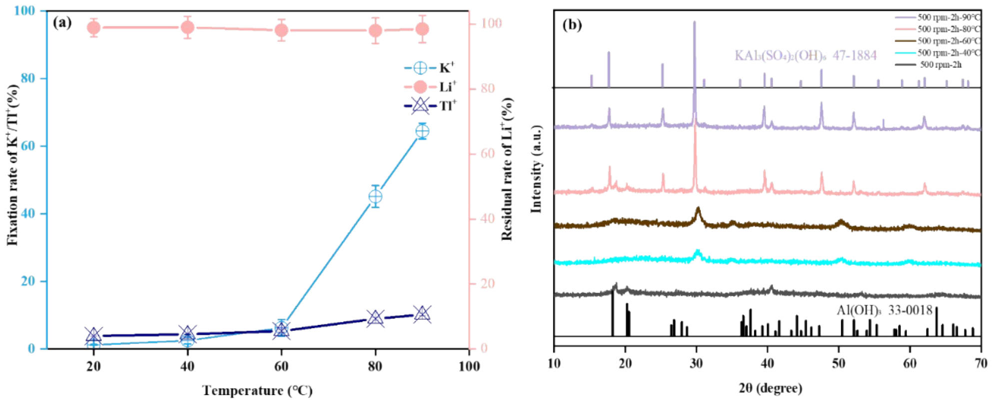

Figure. S17 Effect of reaction temperature and the XRD patterns of the corresponding products

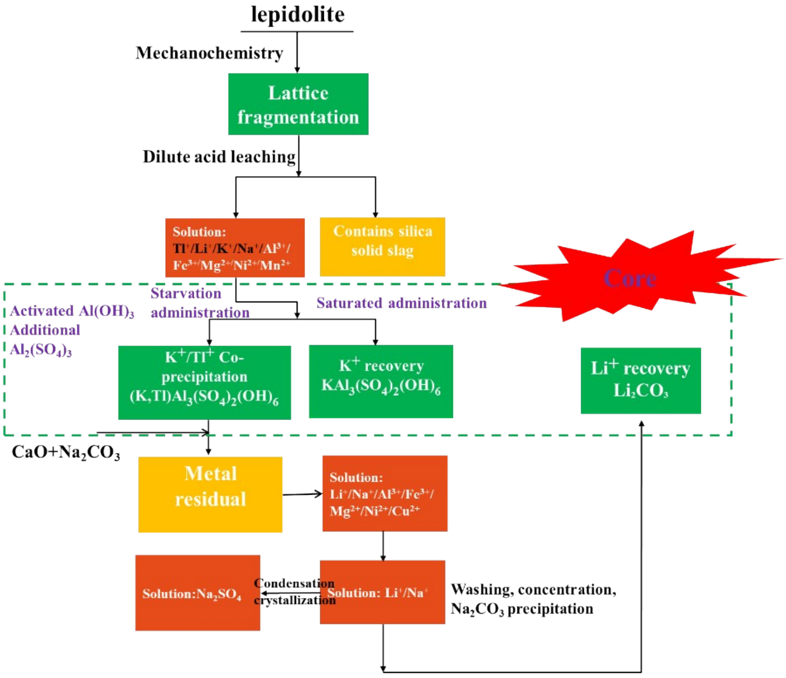

Figure. S18 Conceptual diagram of co-precipitation for K^+/Tl^+ removal or K^+ recovery for practical applications.

Test. 13 Definition of SI

SI is defined as SI = log(IAP/K_{sp}), where IAP is the ion activity product and K_{sp} is the solubility product constant. A positive SI indicates supersaturation (precipitation favorable), while a negative SI indicates undersaturation.

Table S9. SI of alunite and Tl-alunite under different K^+ conditions

Condition	Molar ratio	SI (K-alunite)	SI (Tl-alunite)	Observation (removal rate)
K^+-excess	8:2:3	1.8	-0.2	Rapid K-alunite, Tl^+ <15%
K^+-sufficient	8:2:2	1.2	-0.1	K-alunite, Tl^+ ~12-15%
Starved state	8:2:1	-0.3	+0.4	K^+ and Tl^+ co-precipitation >98%
K^+-absent	8:2:0	-2.1	-1.5	No precipitation, Tl^+ removal <1%

Text S14. Effect of coexisting ions on Tl^+ coprecipitation

To evaluate the practical applicability of the alunite-based coprecipitation method, the influence of common coexisting ions (Fe^{3+}, Na^+, Mg^{2+}, Ca^{2+}) on Tl^+ removal was investigated under optimized conditions: $Al(OH)_3/Al_2(SO_4)_3/K_2SO_4$ molar ratio 8:2:1, 90 °C, 2 h (Initial Tl^+ concentration was 5 mg/L). Competing ions were added at a concentration of 100 mg/L, which is representative of the actual leach solution composition (Table S5). After reaction, the solution was filtered through a 0.22 μm membrane, and the residual Tl^+ and K^+ concentrations were measured by ICP-MS. The results are presented in Table S10.

The data show that Na^+, Mg^{2+}, and Ca^{2+} have negligible effects on Tl^+ removal, with efficiencies remaining >98%. Ferric iron shows a moderate inhibitory effect, reducing Tl^+ removal to approximately 85%. This is likely due to the formation of jarosite-type phases (e.g., $KFe_3(SO_4)_2(OH)_6$) or Fe(III) hydroxide precipitation, which compete for SO_4^{2-} and Al^{3+}. In practical applications, this can be mitigated by adjusting the reagent dosage or by pre-treatment (e.g., pH adjustment) to remove Fe^{3+} prior to the Tl removal step.

Table S10: Effect of coexisting ions on Tl^+ coprecipitation

Competing ion	Concentration (mg/L)	Tl^+ removal (%)	K^+ removal (%)
No competing ions (control)	-	99.2 ± 0.3	99.1 ± 0.4
Fe^{3+}	100	85.25 ± 1.2	96.8 ± 0.6
Na^+	100	98.88 ± 0.4	98.5 ± 0.5
Mg^{2+}	100	99.28 ± 0.1	98.9 ± 0.4
Ca^{2+}	100	98.23 ± 0.5	98.2 ± 0.5

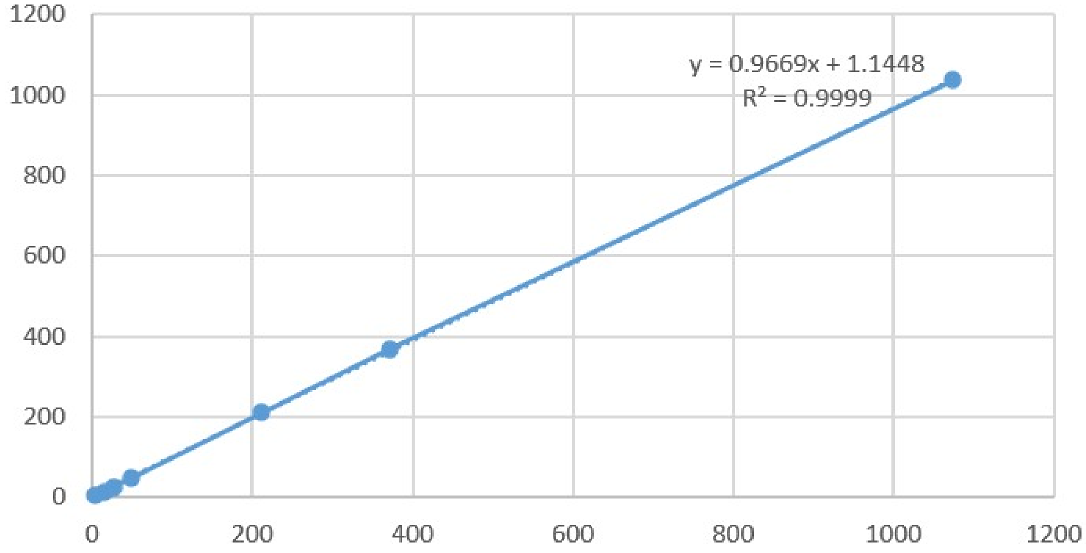

Figure. S19: linear increasing pattern with the increase of initial Tl^+ concentration

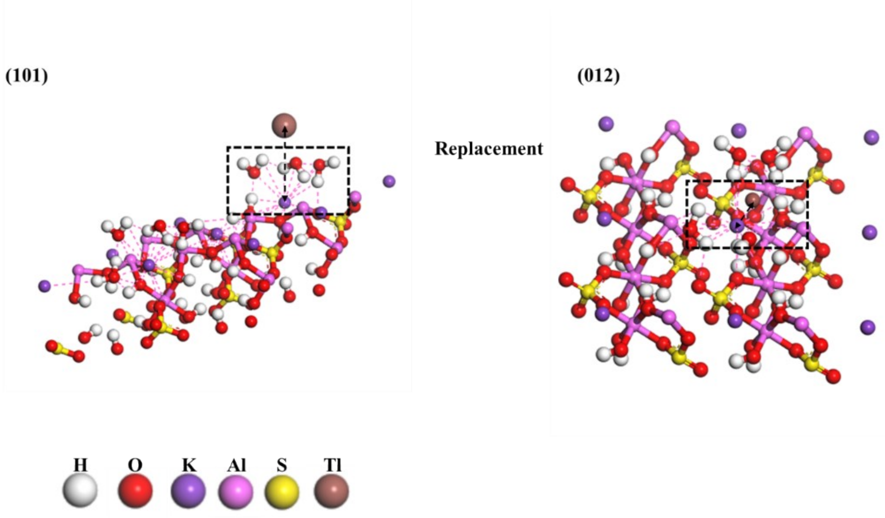

Figure. S20: Tl^+ substitution with $K\text{-}(H_2O)_n^+$ at 101 and 012 crystal planes

Test. 15 Rietveld refinement

Rietveld refinement was performed using the GSAS-II software package. The hexagonal alunite structure (space group $R\bar{3}$*m*, JCPDS No. 47–1884) was used as the starting model. The A-site (Wyckoff position 3a, coordinates 0,0,0) was modeled with mixed occupancy of K^+ and Tl^+, while the Al, S, O, and OH sites were refined with full occupancy. Background was modeled using a Chebyshev polynomial, and peak profiles were fitted using the Thompson-Cox-Hastings function. The refinement converged with good statistics (Rwp < 10%, $\chi^2 < 3$) for all samples. The refined lattice parameters and Tl occupancies are presented in Table S11. The systematic decrease in lattice parameters with increasing Tl occupancy confirms that Tl^+ is incorporated into the alunite structure, substituting for K^+ at the A-site. The slight reversal at the highest Tl concentration (1000 mg/L) is attributed to the coexistence of a minor poorly crystalline secondary phase ($TlAl(SO_4)_2 \cdot 12H_2O$), as evidenced by Raman and XPS analyses (Fig. 4c and 4e).

Table S11. Rietveld refinement results for (K,Tl)-alunite samples

Sample	a (Å)	c (Å)	V (Å³)	Tl occupancy (A-site)	Rwp (%)	χ^2
K-alunite	7.0212(3)	17.483(2)	746.8(1)	0	8.24	2.12
200-Tl-alunite	7.0085(4)	17.445(3)	742.1(2)	0.12(2)	8.56	2.31
400-Tl-alunite	6.9968(5)	17.402(4)	737.5(3)	0.23(3)	8.89	2.45
1000-Tl-alunite	7.0156(6)	17.468(5)	744.2(4)	0.19(4)	9.12	2.68

Table S12. Quantitative EXAFS fitting results for Tl L_3-edge

Sample	Shell	CN	R (Å)	σ^2 ($\times 10^{-3}$ Å²)	ΔE_0 (eV)	R-factor
200-Tl-alunite	Tl–O	4.8(6)	2.87(2)	4.2(8)	1.2(5)	0.012
	Tl–Al	3.2(4)	3.48(3)	6.5(1.2)		
	Tl–S	2.1(3)	3.65(4)	5.8(1.1)		
1000-Tl-alunite	Tl–O	4.6(5)	2.83(2)	5.6(1.0)	1.5(6)	0.018
	Tl–Al	2.5(4)	3.42(3)	7.2(1.4)		
	Tl–S	1.6(3)	3.58(4)	6.9(1.3)		

Text S16. Cost comparison (mechanochemical leaching vs conventional roasting)

To provide a more comprehensive economic perspective, the cost of the mechanochemical leaching step (ball milling + 4% H_2SO_4 leaching) was estimated and compared with that of conventional high-temperature roasting. As summarized in Table S7, the material and energy costs for the mechanochemical route are approximately \$4.08 per cubic meter of leach solution, based on an estimated energy consumption of 25 kWh/t ore and a solid-to-liquid ratio of 1:100. This cost covers the mechanical activation and dilute acid leaching steps.

For conventional roasting processes, the cost structure is substantially different. High-temperature roasting (800–1000 °C) requires significant thermal energy input, typically derived from fossil fuel combustion, in addition to the use of concentrated H_2SO_4 and subsequent off-gas treatment to capture volatile pollutants such as Tl. According to literature reports and industrial practice, the total operating cost for conventional roasting-based lithium extraction from lepidolite ranges from \$15 to \$30 per cubic meter of leach solution, depending on energy prices, acid consumption, and waste treatment requirements[25,26]. This estimate includes fuel costs for roasting, concentrated acid consumption, and the treatment of acidic off-gas and wastewater.

Notably, the mechanochemical route achieves lithium extraction efficiencies exceeding 99% while operating at room temperature with only 4% H_2SO_4, eliminating the need for high-temperature operations and concentrated acid handling. The subsequent Tl removal via alunite coprecipitation adds only approximately \$0.4/m^3 in chemical costs (as shown in Table S7). Therefore, the combined cost for lithium extraction and Tl immobilization using the proposed approach remains significantly lower than the estimated cost of conventional roasting alone.

These cost estimates, together with the energy consumption comparison provided in Table S13 and Text S16, underscore the economic and environmental advantages of the mechanochemical route as a cleaner alternative for lepidolite processing.

Table. S13 Cost Estimation and Calculation Process of Various Methods

Material/Method	Cost Calculation Process	Estimated Cost (\$/m^3)
Prussian blue-Fe_3O_4	Magnetic nanocomposite material, based on Fe_3O_4 market price (~\$50/kg) × dosage 0.2 kg/m^3	10
Fe-Ti-RGO	Graphene composite material, based on RGO cost (~\$100/kg) × dosage 0.1 kg/m^3	10
Poly $AlCl_3$	High-efficiency poly aluminum coagulant, market price (~\$1.2/kg) × typical dosage 8 kg/m^3	9.6
Al can waste-Fe	Recycled aluminum waste with acid dissolution cost (~\$0.3/kg) × dosage 5 kg/m^3	5.5
Fe^0-PS	Zero-valent iron (~2/kg)×2kg+persulfate(2/*kg*)×2*kg*+*persulfate*(3/kg) × 1 kg	7
$KMnO_4$	Conventional oxidant, market price (~\$1.6/kg) × typical dosage 1 kg/m^3	7.6
Alunite structure	**Ball milling + 4% H_2SO_4 leaching(25 kWh/t ore, S/L=1:100→\$4.08)+ Tl coprecipitation chemicals (0.4~\$)**	**4.48**

Table. S14 Comparison of monovalent cation immobilization via the coprecipitation

Ion	Ionic radius (Å)	Initial concentration (mg/L)	Fixed efficiency (%)	Precipitate phase
NH_4^+	1.43	50	99.9 ± 0.1	(NH_4, K) -alunite
Cs^+	1.67	50	92.5 ± 0.8	(Cs, K)-alunite
Rb^+	1.52	50	93.5 ± 0.4	(Rb, K)-alunite
Tl^+*	1.50	50	99.2 ± 0.3	(Tl, K)-alunite

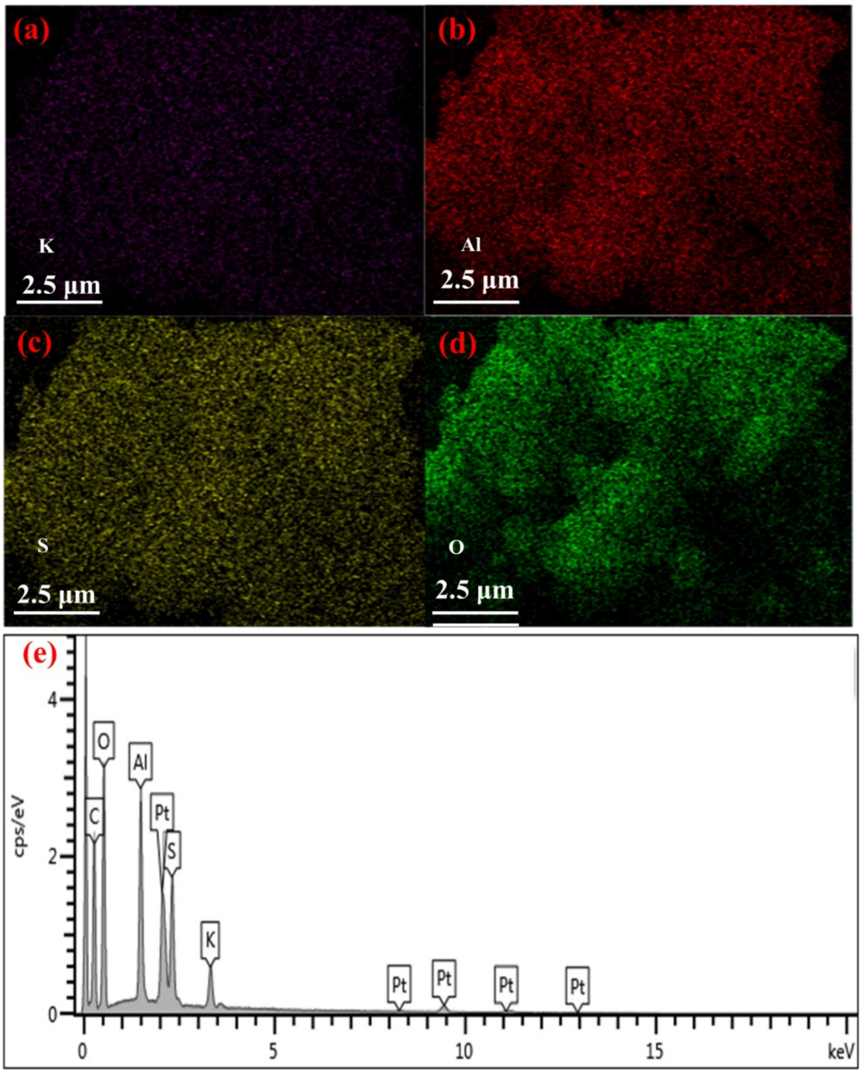

Figure. S21: The distribution of chemical elements on the surface of alunite

References

(1) Xu, L.; Hu, Q.; Liu, Z.; Jian, M.; Peng, Y.; Shen, R.; Liao, W.; Zhong, A. Hydrological alteration drives chemistry of dissolved organic matter in the largest freshwater lake of China (PoYang lake). *Water Research* **2024**, *251*, 121154, DOI: 10.1016/j.watres.2024.121154.

(2) Mei, X.; Dai, Z.; Du, J.; Cheng, J. Three gorges dam enhanced organic carbon burial within the sediments of PoYang lake, china. *Catena* **2024**, *238*, 107859, DOI: 10.1016/j.catena.2024.107859.

(3) Martin, L. A.; Wissocq, A.; Benedetti, M. F.; Latrille, C. Thallium (Tl) sorption onto illite and smectite: implications for Tl mobility in the environment. *Geochim. Cosmochim. Acta* **2018**, *230*, 1-16, DOI: https://doi.org/10.1016/j.gca.2018.03.016.

(4) Shi, Z.; Zhang, P.; Li, X.; Zheng, Y.; Huang, J.; Wang, Y.; Luo, X.; Zhang, G.; Xiao, T.; Long, J.; et al. Thallium removal from wastewater using sulfidized zero-valent manganese: effects of sulfidation method and liquid nitrogen pretreatment. *Chemosphere* **2023**, *318*, 137971, DOI: https://doi.org/10.1016/j.chemosphere.2023.137971.

(5) Liu, Z.; Dai, X.; He, J.; Chen, W.; Wei, Y.; Zhou, Q.; Ma, D.; Zheng, X. Unraveling the thallium immobilization in CuO/PMS system. *Chem. Eng. J.* **2023**, *472*, 144869, DOI: 10.1016/j.cej.2023.144869.

(6) López, Y. C.; Ortega, G. A.; Martínez, M. A.; Reguera, E. Magnetic Prussian blue derivative like absorbent cages for an efficient thallium removal. *J. Clean. Prod.* **2021**, *283*, 124587, DOI: 10.1016/j.jclepro.2020.124587.

(7) Shi, Y.; Huang, L.; Mahmud, S.; Zhang, G.; Li, H.; Wang, Y.; Xiao, T.; Zeng, Q.; Liu, Z.; Yu, H.; et al. High-efficiently capturing trace thallium (ι) from wastewater via the Prussian blue@polytetrafluoroethylene hybrid membranes. *Chem. Eng. J.* **2023**, *451*, 138712, DOI: 10.1016/j.cej.2022.138712.

(8) Li, L.; Liu, C.; Ma, R.; Yu, Y.; Chang, Z.; Zhang, X.; Yang, C.; Chen, D.; Yu, Y.; Li, W.; et al. Enhanced oxidative and adsorptive removal of thallium (Tl) using Fe_3O_4@TiO_2 decorated rgo nanosheets as persulfate activator and adsorbent. *Sep. Purif. Technol.* **2021**, *271*, DOI: 10.1016/j.seppur.2021.118827.

(9) Chen, W.; Xiong, J.; Liu, J.; Wang, H.; Yao, J.; Liu, H.; Huangfu, X.; He, Q.; Ma, J.; Liu, C.; et al. Thermodynamic and kinetic coupling modeling for thallium sorption at a heterogeneous titanium dioxide interface. *J. Hazard. Mater.* **2022**, *428*, 128230, DOI: 10.1016/j.jhazmat.2022.128230.

(10) Chen, K.; Tzou, Y.; Hsu, L.; Guo, J.; Cho, Y.; Teah, H.; Hsieh, Y.; Liu, Y. Oxidative removal of thallium(I) using Al beverage can waste with amendments of Fe: Tl speciation and removal mechanisms. *Chem. Eng. J.* **2022**, *427*, 130846, DOI: https://doi.org/10.1016/j.cej.2021.130846.

(11) Wan, S.; Song, X.; Wang, X.; Yuan, C.; Wang, B.; Chen, H.; Li, Y.; Ouyang, K.; Chen, R. Enhanced removal thallium from rinsing wastewater by poly aluminum chloride: experimental and theoretical studies. *Sep. Purif. Technol.* **2022**, *302*, 122158, DOI: https://doi.org/10.1016/j.seppur.2022.122158.

(12) Fang, F.; Li, N.; Zhang, X.; Liu, J.; Beiyuan, J.; Cao, J.; Wang, J.; Liu, Y.; Song, G.; Xiao, T. Perspective on Fe^0-PS synergetic effect and reaction mechanism in the thallium(I) contaminated water treatment. *Environ. Res.* **2022**, *214*, 113698, DOI: https://doi.org/10.1016/j.envres.2022.113698.

(13) Huang, Y.; Liu, Z.; Liu, H.; Ma, C.; Chen, W.; Huangfu, X. Removal of thallium by MnO_x coated

limestone sand filter through regeneration of $KMnO_4$: combination of physiochemical and biochemical actions. *J. Hazard. Mater.* **2024**, *464*, 132947, DOI: https://doi.org/10.1016/j.jhazmat.2023.132947.

(14) Tian, C.; Zhang, B.; Borthwick, A. G. L.; Li, Y.; Liu, W. Electrochemical oxidation of thallium (I) in groundwater by employing single-chamber microbial fuel cells as renewable power sources. *Int. J. Hydrog. Energy* **2017**, *42*(49), 29454-29462, DOI: https://doi.org/10.1016/j.ijhydene.2017.10.026.

(15) Chao, W.; Huimin, H.; Min, C.; Junwei, H.; Lei, P.; Qian, W.; Qing, S.; Tingting, Z.; Qiwu, Z. Active ion-exchangeable $Bi_2O(OH)_2SO4$ synthesized by ball milling for effective iodine enrichment: insight into the pathway. *J. Nucl. Mater.* **2022**, *572*, 154081, DOI: 10.1016/j.jnucmat.2022.154081.

(16) Wang, C.; Hu, H.; Chen, M.; Huang, J.; Shi, Q.; Zeng, C.; Deng, Z.; Zhang, Q. Efficient stabilization of Barium- and gypsum-bearing tailings by one-step dry ball milling—an ingenious inspiration. *Sep. Purif. Technol.* **2023**, *313*, 123473, DOI: https://doi.org/10.1016/j.seppur.2023.123473.

(17) Wang, C.; Hu, H.; Chen, M.; Wang, Q.; Liu, C.; Chen, M.; Yan, S.; Zhang, Q. Mechanochemical synthesis of bismuth-based anion exchange materials to immobilize arsenic pollution - prospects for advanced treatment of anion-containing wastewater. *J. Clean. Prod.* **2022**, *340*, 130747, DOI: https://doi.org/10.1016/j.jclepro.2022.130747.

(18) Chakraborty, S.; Bardelli, F.; Charlet, L. Reactivities of Fe(II) on calcite: selenium reduction. *Environ. Sci. Technol.* **2010**, *44*(4), 1288-1294, DOI: 10.1021/es903037s.

(19) Wang, Z.; Li, J.; Yin, L.; Zhang, L.; Liu, J.; Shen, N.; Yan, S.; Guan, Q. A new procedure for separating thallium from geological materials prior to stable isotope ratio determination by MC–ICP–MS. *Chem. Geol.* **2023**, *627*, 121457, DOI: 10.1016/j.chemgeo.2023.121457.

(20) Du, Y.; Shi, L.; Li, X.; Liu, J.; Ying, R.; Hu, P.; Wu, L.; Christie, P. Potential mobilization of water-dispersible colloidal thallium and arsenic in contaminated soils and sediments in mining areas of southwest china. *J. Hazard. Mater.* **2024**, *465*, 133211, DOI: 10.1016/j.jhazmat.2023.133211.

(21) Chen, X.; Wang, C.; Chen, M.; Hu, H.; Huang, J.; Jiang, T.; Zhang, Q. Enhanced Cd^{2+} removal from aqueous solution using olivine and magnesite combination: new insights into the mechanochemical synergistic effect. *J. Environ. Sci.* **2025**, *147*, 714-725, DOI: https://doi.org/10.1016/j.jes.2023.10.038.

(22) Hu, H.; Zhang, Q.; Wang, Q.; Chen, M.; Wang, C.; Wang, Z. Rapid mechanochemical dichlorination of hexachlorobenzene with zero-valent silicon as a novel additive: the attempt of zero-valent nonmetallic. *Journal of Environmental Chemical Engineering* **2023**, *11*(6), 111398, DOI: https://doi.org/10.1016/j.jece.2023.111398.

(23) Luo, S.; Zhao, X.; Qu, Y.; Wang, L.; Zhou, B.; Si, W.; Fang, W. Insights into the full cycling of oxygen in vocs oxidation on α-MnO_2: a Nap-XPS study. *Appl. Surf. Sci.* **2023**, *634*, 157506, DOI: 10.1016/j.apsusc.2023.157506.

(24) Fan, D.; Anitori, R. P.; Tebo, B. M.; Tratnyek, P. G.; Lezama Pacheco, J. S.; Kukkadapu, R. K.; Kovarik, L.; Engelhard, M. H.; Bowden, M. E. Oxidative remobilization of technetium sequestered by sulfide-transformed nano zerovalent iron. *Environ. Sci. Technol.* **2014**, *48*(13), 7409-7417, DOI: 10.1021/es501607s.

(25) Tian-Ming, G.; Na, F.; Wu, C.; Tao, D. Lithium extraction from hard rock lithium ores (spodumene, lepidolite, zinnwaldite, petalite): technology, resources, environment and cost. *China Geol.* **2023**, *6*(1), 137-153, DOI: 10.31035/cg2022088.

(26) Zhou, Y.; Tang, X.; Qing, D.; Li, J.; Wang, H. Research progress of technology of lithium extraction. *Sep. Purif. Technol.* **2025**, *359*, 130561, DOI: 10.1016/j.seppur.2024.130561.